

# Domain-Agnostic Stroke Lesion Segmentation Using Physics-Constrained Synthetic Data

Liam Chalcraft<sup>1</sup>, Jenny Crinion<sup>2</sup>, Cathy J. Price<sup>1</sup>, John Ashburner<sup>1</sup>

<sup>1</sup> Department of Imaging Neuroscience, University College London

<sup>2</sup> Institute of Cognitive Neuroscience, University College London  
l.chalcraft@cs.ucl.ac.uk

**Abstract.** Segmenting stroke lesions in Magnetic Resonance Imaging (MRI) is challenging due to diverse clinical imaging domains, with existing models struggling to generalise across different MRI acquisition parameters and sequences. In this work, we propose two novel physics-constrained approaches using synthetic quantitative MRI (qMRI) images to enhance the robustness and generalisability of segmentation models. We trained a qMRI estimation model to predict qMRI maps from MPRAGE images, which were used to simulate diverse MRI sequences for segmentation training. A second approach built upon prior work in synthetic data for stroke lesion segmentation, generating qMRI maps from a dataset of tissue labels. The proposed approaches improved over the baseline nnUNet on a variety of out-of-distribution datasets, with the second approach outperforming the prior synthetic data method.

## 1 Introduction

Segmenting brain pathologies in MRI is crucial for research and clinical applications but remains challenging due to the diversity of hospital imaging domains. Public datasets and benchmarks achieve high performance across pathologies but rely on consistent imaging sequences, such as T1-weighted (T1w), T2-weighted (T2w), and FLAIR, with similar parameters (e.g., echo time and flip angle). Even multi-site studies select data with overlapping sequences [22], limiting assessments to like-for-like comparisons: models trained on isotropic T1w are tested only on isotropic T1w, or co-registered T1w and T2w are tested together. In clinical settings, however, test domains rarely match training domains, creating a need for open-domain models capable of handling diverse MRI acquisitions.

Domain adaptation methods often assume specific target domains during training [10] or require many unlabelled target images at test time [26], neither of which suits clinical workflows, where only a single image may be available at test time. Domain-agnostic approaches, such as SynthSeg [3], which uses label-conditioned Gaussian Mixture Models (GMMs) to generate synthetic images with randomised tissue contrasts, have shown moderate success for lesion segmentation [2]. While effective for healthy tissue segmentation, SynthSeg struggles with pathologies like stroke, where lesions are heterogeneous and complex.

Random sampling often produces unrealistic images, leading to poor generalisation, as demonstrated in [8], where models trained on synthetic data alone performed poorly in-domain. The lack of physical realism in synthetic images prevents models from learning true tissue relationships, causing errors on real clinical images.

To address these limitations, we propose generating synthetic images constrained by quantitative MRI (qMRI) parameters and forward models of MRI sequences, ensuring physical plausibility. qMRI provides voxel-level tissue properties, including proton density (PD), longitudinal relaxation rate ( $R_1$ ), effective transverse relaxation rate ( $R_2^*$ ), and magnetisation transfer (MT). Using qMRI maps, we can simulate diverse MRI sequences while preserving tissue properties, producing synthetic images that are both varied and physically accurate, potentially improving model generalisation.

Despite its promise, qMRI acquisition is time-consuming, requiring multiple scans with specific sequences, which is impractical in time-critical settings like stroke. Consequently, qMRI data are scarce for training deep learning models. To overcome this, deep learning methods now estimate qMRI maps from standard sequences. Supervised approaches use real qMRI maps to synthesise images via forward models [5, 25], while unsupervised methods predict qMRI parameters from real images and validate them against input images via forward models [4]. These approaches enable qMRI generation without specialised acquisitions, making it feasible for synthetic data generation.

We propose two novel methods leveraging qMRI for domain-agnostic stroke lesion segmentation. The first, **qATLAS**, trains a qMRI estimation model to predict qMRI maps from MPRAGE images, commonly used in public datasets, enabling augmentation of the ATLAS dataset [18] with qMRI maps to simulate diverse MRI sequences while preserving acquisition physics. The second, **qSynth**, extends [8] by sampling synthetic qMRI maps from intensity priors derived from real qMRI data. Unlike methods that randomly sample intensities, qSynth ensures physical realism by generating qMRI maps and simulating sequences using forward models. This allows creation of large, physically plausible qMRI datasets for deep learning, improving stroke lesion segmentation on diverse imaging domains.

By incorporating qMRI into synthetic data generation, we bridge the gap between synthetic and clinical data. Our physics-constrained augmentation ensures simulated images respect MRI physics, producing models that generalise across sequences and acquisition parameters while remaining robust in clinical settings.

## 2 Methods

We propose two methods, **qATLAS** and **qSynth**, for domain-agnostic stroke lesion segmentation. Both leverage qMRI parameter maps to generate diverse, physics-constrained training data, enhancing robustness and generalisability.

## 2.1 qATLAS: Estimating qMRI from MPRAGE

The **qATLAS** method involves training a qMRI estimation model to predict qMRI parameter maps - Proton Density (PD, arbitrary units), Longitudinal Relaxation Rate ( $R_1$ ,  $s^{-1}$ ), Effective Transverse Relaxation Rate ( $R_2^*$ ,  $s^{-1}$ ), and Magnetisation Transfer (MT, percentage units) - from MPRAGE images. We used a dataset of 51 subjects (22 healthy and 29 stroke patients), split into training and validation sets in an 80:20 ratio. The qMRI maps were estimated using the 3D-EPI method provided by the hMRI toolbox [23].

We simulated MPRAGE images using the NiTorch library, with parameter distributions as follows: repetition time ( $T_R$ ) uniformly distributed in [1.9, 2.5] s, inversion time ( $T_I$ ) in [0.6, 1.2] s, echo time ( $T_E$ ) in [2, 4] ms, flip angle ( $\alpha$ ) in [ $5^\circ$ ,  $12^\circ$ ], and magnetic field strength ( $B_0$ ) in [0.3, 7] T, where  $\mathcal{U}(a, b)$  represents a uniform distribution.

**Data Augmentation:** To enhance the diversity of the training data, we applied several augmentation techniques using the MONAI library [7], including elastic and affine deformations, bias field augmentation, Gibbs ringing, Rician noise addition, and cropping to a size of  $192 \times 192 \times 192$  voxels. Figure 1 illustrates examples of the augmented training data.

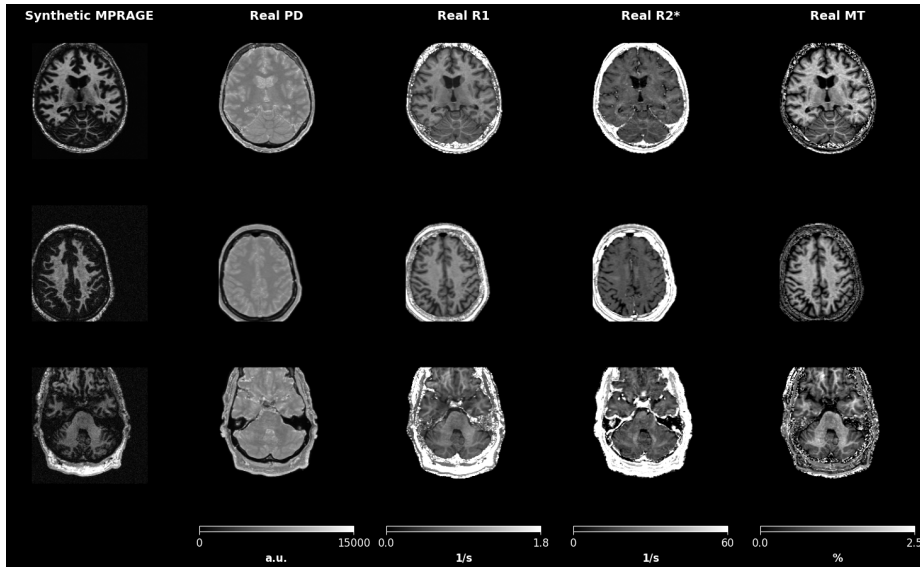


Fig. 1: Examples of training data for qMRI parameter map prediction in the qATLAS method.

**Model Architecture and Training:** We employed a U-Net model based on the nnUNet architecture [16] for the qMRI estimation task. The network consisted of five encoder stages, each containing two residual units with channel

sizes of (24, 48, 96, 192, 384), respectively. The model used GELU activations [14], instance normalisation [24], linear upsampling in the decoder, and a dropout rate of 0.1.

The network predicted four output channels corresponding to the target qMRI maps (PD,  $R_1$ ,  $R_2^*$ , MT). To ensure positivity of the parameter estimates, PD,  $R_1$ , and  $R_2^*$  were obtained by applying the exponential function to the respective network outputs. The MT map was estimated using following function:

$$\text{MT} = \frac{100}{1 + \exp(-f(\mathbf{x}))} \quad (1)$$

where  $f(\mathbf{x})$  is the network output for the MT channel.

The model was trained for a total of 200,000 iterations with a batch size of 1, using the AdamW optimiser [19] with a learning rate of  $10^{-4}$  and parameters  $\beta_1 = 0.9$ ,  $\beta_2 = 0.999$ , and weight decay  $\lambda = 0.01$ . For the first 20,000 iterations, we used the L2 loss function. Subsequently, we employed a combined loss function inspired by [1], which included L1 and L2 losses on both the predictions and their spatial gradients:

$$\mathcal{L}(\mathbf{y}, \hat{\mathbf{y}}) = \text{L1}(\mathbf{y}, \hat{\mathbf{y}}) + \text{L2}(\mathbf{y}, \hat{\mathbf{y}}) + \text{L1}(\nabla\mathbf{y}, \nabla\hat{\mathbf{y}}) + \text{L2}(\nabla\mathbf{y}, \nabla\hat{\mathbf{y}}) \quad (2)$$

where  $\mathbf{y}$  is the ground truth,  $\hat{\mathbf{y}}$  is the prediction, and  $\nabla$  denotes the spatial gradient.

Additionally, we incorporated a perceptual loss based on the LPIPS metric [28], using a pre-trained Med3D model [9]. The perceptual loss  $\text{PL}(\mathbf{y}, \hat{\mathbf{y}})$  was weighted by a factor of 0.1 relative to the main reconstruction loss.

Figure 2 shows examples of the predicted qMRI parameter maps from input MPRAGE images in the ATLAS dataset [18].

**Simulation of MRI Sequences:** Using the estimated qMRI maps from the ATLAS dataset, we simulated a wide range of MRI sequences with varied acquisition parameters via a physics-based generative model (see Section 2.3). This resulted in the **qATLAS** dataset, which we used to train the segmentation model.

## 2.2 qSynth: Synthesizing qMRI Maps from Tissue Labels

The **qSynth** method involves generating synthetic qMRI parameter maps by sampling synthetic intensities for tissue labels from qMRI intensity priors. Instead of estimating qMRI maps from MPRAGE images, we use label-conditioned GMMs to synthesise qMRI maps directly from segmentation labels. This approach allows us to create a diverse set of qMRI maps without relying on real MRI data.

**Generation of Synthetic qMRI Maps:** We defined prior distributions for the qMRI parameters (PD,  $R_1$ ,  $R_2^*$ , MT) for different tissue types (gray matter, white matter, cerebrospinal fluid, and lesions) based on the population used for the parameter estimation model in qATLAS. For each tissue, per-subject

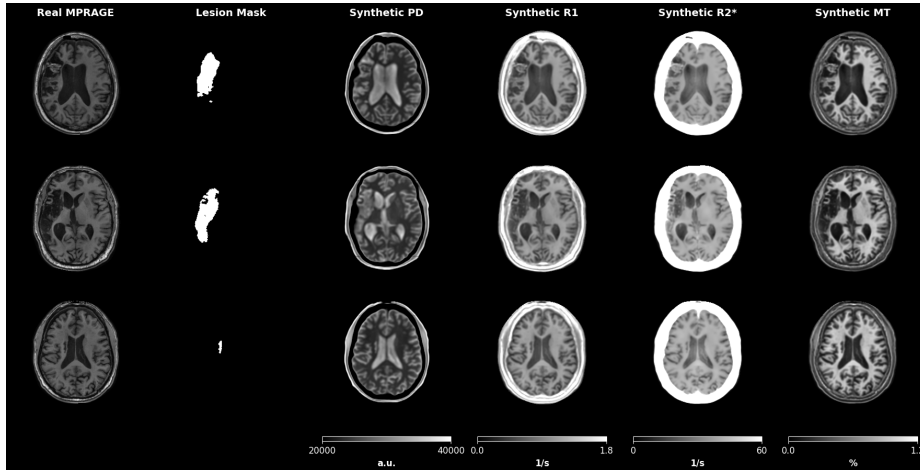


Fig. 2: Examples of predicted qMRI parameter maps from input MPRAGE images of the ATLAS dataset in the qATLAS method.

distribution parameters  $(\mu, \beta)$  were estimated, and then a population-level distribution parametrised by  $(\mu_\mu, \mu_\sigma, \sigma_\mu, \sigma_\sigma)$ . For any tissue or lesion classes where real data is not available, it is feasible that this prior could be approximated from literature values. For each tissue label in the segmentation maps, we sampled the qMRI parameters from the corresponding priors to create synthetic qMRI maps. This method ensures that the synthesised qMRI maps accurately reflect the realistic range of tissue properties. All healthy tissue classes were acquired using the Multibrain SPM toolbox [6] to obtain classes of Gray Matter (GM), White Matter (WM), GM/WM partial volume, Cerebrospinal Fluid (CSF) and several non-brain tissues.

**Simulation of MRI Sequences:** Using the synthesised qMRI maps, we simulated MRI images across various sequences and acquisition parameters using the physics-based generative model described in Section 2.3. This resulted in the **qSynth** dataset, which we used to train an alternative segmentation model.

### 2.3 Physics-Based Generative Model

Both qATLAS and qSynth methods use a physics-based generative model to simulate realistic MRI images from qMRI parameter maps. The simulation relies on signal equations that model the signal intensity based on tissue properties and sequence parameters.

**Signal Equations:** The simulation of MRI images from qMRI parameter maps relies on signal equations for various MRI sequences. We considered several common MRI sequences, each described by its respective signal equation:

*Fast Spin-Echo (FSE):*

$$S_{\text{FSE}} = B_1 \cdot \text{PD} \cdot (1 - e^{-R_1 \cdot T_R}) \cdot e^{-R_2 \cdot T_E} \quad (3)$$

*Gradient-Echo (GRE):*

$$S_{\text{GRE}} = B_1 \cdot \text{PD} \cdot \sin(\alpha) \cdot \frac{1 - e^{-R_1 \cdot T_R}}{1 - \cos(\alpha) \cdot e^{-R_1 \cdot T_R}} \cdot e^{-R_2^* \cdot T_E} \quad (4)$$

*Fluid-Attenuated Inversion Recovery (FLAIR):*

$$S_{\text{FLAIR}} = B_1 \cdot \text{PD} \cdot e^{-R_2 \cdot T_E} \cdot (1 - 2 \cdot e^{-R_1 \cdot T_I} + e^{-R_1 \cdot T_R}) \quad (5)$$

*Magnetisation-Prepared Rapid Gradient Echo (MPRAGE):*

$$S_{\text{MPRAGE}} = \left| \sin(\alpha) \cdot \left[ \frac{1 - e^{-R_1 \cdot T_R}}{1 - \cos(\alpha) \cdot e^{-R_1 \cdot T_R}} \cdot \left( 1 - (\cos(\alpha) \cdot e^{-T_X \cdot R_1})^n \right) \right] \cdot e^{-T_D \cdot R_1} + (1 - e^{-T_D \cdot R_1}) \right| \quad (6)$$

In these equations,  $B_1$  represents the receive field strength,  $\alpha$  is the flip angle (in radians),  $T_R$  is the repetition time,  $T_E$  is the echo time,  $T_I$  is the inversion time,  $T_X$  is the excitation repetition time,  $T_D$  is the delay time, and  $n$  is the number of excitation pulses. All times are in seconds unless otherwise specified.

**Noise Simulation:** To simulate realistic MRI data, we added Rician noise to the generated images, modeling the noise characteristics of magnitude MRI data [12]. The noisy signal  $S_{\text{noisy}}$  was computed as:

$$S_{\text{noisy}} = \sqrt{(S_{\text{MRI}} + \mathcal{N}(0, \sigma^2))^2 + (\mathcal{N}(0, \sigma^2))^2} \quad (7)$$

where  $S_{\text{MRI}}$  is the simulated signal without noise, and  $\mathcal{N}(0, \sigma^2)$  represents a zero-mean Gaussian distribution with variance  $\sigma^2$ , simulating the real and imaginary noise components.

All signal simulations and noise additions were performed using the NiTorch library<sup>‡</sup>.

**Acquisition Parameters and Data Augmentation:** We simulated a wide range of MRI sequences with diverse acquisition parameters. The sequences and their respective parameter distributions were as follows:

- **FLAIR:**  $T_E \sim 10^{\mathcal{N}(\log_{10} 0.02, \log_{10} 0.1)}$  s,  $T_R \sim 10^{\mathcal{U}(\log_{10} 0.001, \log_{10} 5)}$  s,  $T_I \sim 10^{\mathcal{U}(\log_{10} 0.001, \log_{10} 3)}$  s
- **FSE:**  $T_E \sim 10^{\mathcal{U}(\log_{10} 0.001, \log_{10} 3)}$  s,  $T_R \sim 10^{\mathcal{U}(\log_{10} 0.001, \log_{10} 3)}$  s
- **MPRAGE:**  $T_R \sim \mathcal{N}(23, 2.3)$  s,  $T_I \sim \mathcal{U}(0.6, 0.9)$  s,  $T_X \sim \mathcal{U}(0.004, 0.008)$  s,  $T_E \sim \mathcal{U}(0.002, 0.004)$  s,  $\alpha \sim \mathcal{U}(5^\circ, 12^\circ)$
- **GRE:**  $T_E \sim 10^{\mathcal{U}(\log_{10} 0.002, \log_{10} 0.08)}$  s,  $T_R \sim 10^{\mathcal{U}(\log_{10} 0.005, \log_{10} 5)}$  s,  $\alpha \sim \mathcal{U}(5^\circ, 50^\circ)$

<sup>‡</sup><https://github.com/balbasty/nitorch>

Here,  $\mathcal{N}(\mu, \sigma^2)$  denotes a normal distribution with mean  $\mu$  and standard deviation  $\sigma$ . The sequences were randomly selected with equal probability during training, and the absolute values of sampled parameters were used to ensure physical plausibility.

To further augment the data, we applied random elastic deformations, multiplicative bias field augmentations, random axis flips, Gaussian noise addition, low-resolution reslicing, and random cropping to a size of  $192 \times 192 \times 192$  voxels, using the MONAI library. Un-augmented data samples are shown for the three methods in Figure 3.

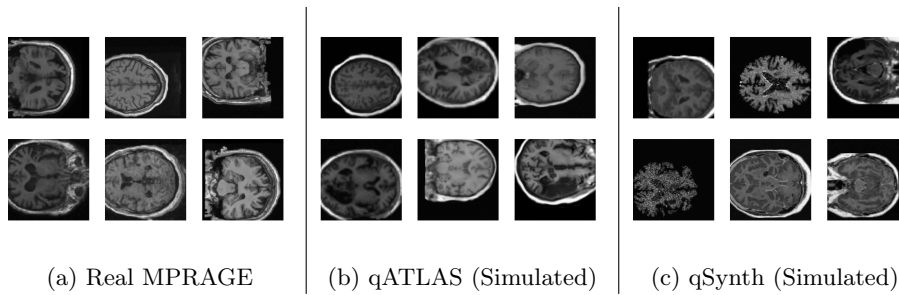


Fig. 3: Samples of T1-weighted MPRAGE training images from the real source dataset (3a), qATLAS data sampling (3b) and qSynth data sampling (3c).

## 2.4 Segmentation Model Training

We trained nnUNet-based segmentation models [16] using both the qATLAS and qSynth datasets. Both methods are considered equally valid options for training domain-agnostic segmentation models. As baseline comparisons, we also train a model on the real MPRAGE images from the ATLAS dataset, as well as a standard synthetic data model using the public implementation of [8] (referred to here as ‘Synth’). For both Synth and qSynth, we also show results for models trained with a mix of the synthetic data and the real ATLAS MPRAGE images.

**Model Architecture and Training Details:** The segmentation models were configured with PReLU activations [13] and one residual unit per block. For the qATLAS model, we predicted two classes: background and stroke lesion. For the qSynth model, trained with synthetic data generated from tissue labels, we predicted additional healthy tissue classes: gray matter (GM), white matter (WM), GM/WM partial volume, and cerebrospinal fluid (CSF).

Baseline and qATLAS models were trained using data from the ATLAS dataset (N=655, 419:105:131 train-val-test split), whilst Synth and qSynth models used the ATLAS lesion labels in combination with Multibrain healthy segmentation labels derived from the OASIS-3 dataset (N=2679, 2579:100 train-val

split). Further details on the generative model used to create images from tissue labels can be found in the original implementation [8].

All models were optimised using a combined Dice and cross-entropy loss function, employing the AdamW optimiser [19] with a learning rate of  $10^{-4}$  and parameters  $\beta_1 = 0.9$ ,  $\beta_2 = 0.999$ , and weight decay  $\lambda = 0.01$ . A learning rate scheduler was applied as  $\eta_n = \eta_0(1 - \frac{n}{N})^{0.9}$ , where  $n$  is the current iteration and  $N$  is the total number of iterations.

All models were trained for 700,000 iterations with a batch size of 1.

### 3 Experiments

Models were validated on several datasets. We evaluated models on the ATLAS hold-out test set (131 subjects, 1mm isotropic MPRAGE) for in-domain evaluation. For out-of-domain robustness, we used the ARC dataset (229 subjects with T2 images, 202 with T1, and 85 with FLAIR) [11, 17]. To further assess out-of-domain robustness in data closer resembling what is seen in a clinical workflow, we used a private dataset of 263 subjects with combinations of T2 and FLAIR images resliced to 2mm isotropic and spatially normalised to the MNI template, referred to here as PLORAS. The ISLES 2015 dataset (28 subjects, multi-modal MRI) [20] assessed model performance on acute lesions, highlighting physiological changes not covered by our augmentations.

At test-time, images are loaded, oriented to RAS, resliced to 1 mm slice thickness, histogram normalised and images z-scored to a zero mean and unit standard deviation. Sliding-window inference was performed using a patch size of  $192 \times 192 \times 192$ , using patches with a 50% overlap and a Gaussian weighting with  $\sigma = 0.125$  when combining patches. Test-time augmentation was additionally performed by averaging logits across all possible combinations of flips in the x, y and z axes. Predicted logits were then resliced to the original input image and a softmax applied to derive posterior probabilities. An argmax was then used to derive a binary lesion map. TTA is a popular heuristic method for increasing model robustness at test-time [27].

**Multi-modal ensembling:** In addition to per-modality evaluation, we provide results of ensembles of per-modality predictions to better represent how such a model may be used in practice. Logits were averaged first across all modalities before taking the softmax and post-processing as stated previously. Ensemble results are reported for ISLES 2015 and ARC datasets.

Comparison to the ground truth was performed by reslicing both the prediction and ground truth to 1 mm slice thickness and padding images to a size of  $256 \times 256 \times 256$ . Segmentations were evaluated using the Dice coefficient and 95th-percentile Hausdorff distance (HD95).

The Dice coefficient measures overlap, where a score of 1 indicates perfect overlap and 0 indicates no overlap. The Hausdorff distance measures surface similarity by determining the shortest distance between surfaces at all given points, using the 95th-percentile value to avoid errors from anomalous values in



imperfect masks. Note that a prediction of entirely background class will return the maximum side length of 256.

## 4 Results

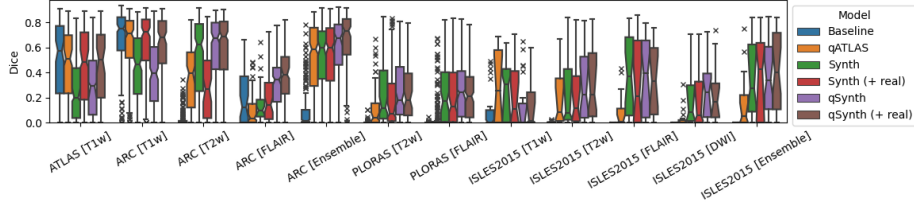


Fig. 4: Dice metric performance for all datasets.

### 4.1 ATLAS

The ATLAS test dataset, a subset of the training data, is considered in-domain. The baseline model is expected to match this data perfectly, while the qMRI generator model needs to have accurately reproduced MPRAGE details during training to match performance. Table 1 shows that the baseline model generally performed better, but differences were not statistically significant (Figure 4) except in Synth/qSynth. qSynth achieves a significant improvement over the Synth model, indicating that the physics-constrained pipeline reduces the domain shift between simulated and real data.

Table 1: Median results on the ATLAS hold-out set (N=131). Best score shown in bold, with second-best underlined and third-best in italics. Student’s  $t$  distribution 95% confidence intervals given in brackets.

Modality	Model	Dice	HD95
T1w	Baseline	<b>0.575 (0.522-0.628)</b>	<b>19.7 (10.2-29.3)</b>
	qATLAS	0.508 (0.460-0.556)	<i>34.4 (26.5-42.2)</i>
	Synth	0.197 (0.155-0.239)	63.7 (59.6-67.9)
	Synth (+ real)	0.482 (0.431-0.534)	22.6 (12.0-33.3)
	qSynth	0.294 (0.250-0.338)	51.3 (43.5-59.2)
	qSynth (+ real)	<i>0.501 (0.450-0.551)</i>	38.0 (28.2-47.8)

### 4.2 ARC

The ARC dataset introduces a moderate domain shift, with T1w data from a different site and larger shifts in T2 and FLAIR modalities. Table 2 and Figure 4 show that the baseline model outperformed qATLAS in Dice and HD95

without statistical significance. For T1w, qSynth initially performed worse than Synth but reached comparable performance after incorporating real data. In T2w, qSynth outperformed all models, with real data integration further improving Dice scores. In both FLAIR and ensemble modalities, qSynth achieved statistically significant improvements over all other models, highlighting its robustness in domain-shifted scenarios.

Table 2: Median results on the ARC dataset (N=229). Best score shown in bold, with second-best underlined and third-best in italics Student’s  $t$  distribution 95% confidence intervals given in brackets.

Modality	Model	Dice	HD95
T1w	Baseline	<b>0.752 (0.713-0.790)</b>	<b>8.8 (2.5-15.0)</b>
	qATLAS	<i>0.710 (0.673-0.747)</i>	<i>11.8 (5.6-18.1)</i>
	Synth	0.467 (0.430-0.504)	57.1 (52.9-61.3)
	Synth (+ real)	0.723 (0.684-0.762)	11.0 (4.0-18.0)
	qSynth	0.394 (0.359-0.429)	31.0 (26.6-35.5)
	qSynth (+ real)	0.683 (0.643-0.723)	13.0 (6.8-19.2)
T2w	Baseline	0.000 (0.000-0.007)	74.4 (71.4-77.4)
	qATLAS	0.395 (0.363-0.426)	54.5 (50.7-58.2)
	Synth	<i>0.626 (0.588-0.665)</i>	<i>46.1 (42.2-50.0)</i>
	Synth (+ real)	0.268 (0.233-0.302)	64.0 (60.5-67.4)
	qSynth	0.674 (0.640-0.709)	<b>39.0 (34.8-43.2)</b>
	qSynth (+ real)	<b>0.691 (0.655-0.726)</b>	43.0 (38.7-47.2)
FLAIR	Baseline	0.122 (0.076-0.169)	58.5 (49.5-67.4)
	qATLAS	0.032 (0.005-0.059)	59.7 (50.7-68.7)
	Synth	0.096 (0.070-0.123)	57.6 (49.2-65.9)
	Synth (+ real)	<i>0.141 (0.097-0.185)</i>	<i>52.2 (43.3-61.1)</i>
	qSynth	0.344 (0.300-0.388)	50.3 (41.3-59.2)
	qSynth (+ real)	<b>0.382 (0.332-0.431)</b>	<b>44.0 (34.5-53.5)</b>
Ensemble	Baseline	0.012 (0.000-0.032)	48.2 (40.1-56.3)
	qATLAS	0.586 (0.549-0.622)	<b>16.4 (10.9-22.0)</b>
	Synth	0.597 (0.562-0.631)	44.0 (39.9-48.2)
	Synth (+ real)	<i>0.602 (0.566-0.638)</i>	20.1 (14.8-25.3)
	qSynth	0.676 (0.642-0.709)	31.6 (27.2-36.0)
	qSynth (+ real)	<b>0.735 (0.701-0.770)</b>	<i>20.7 (16.2-25.2)</i>

### 4.3 PLORAS

The PLORAS dataset, containing real clinical data from UK hospitals, highlights the superiority of qSynth over baseline and qATLAS models as seen in Table 3. qSynth also demonstrated moderate but consistent improvements over Synth, reflecting its capacity to generalise effectively to diverse real-world clinical scenarios.

### 4.4 ISLES 2015

The ISLES 2015 dataset, featuring co-registered T1w, T2w, FLAIR, and DWI channels with acute stroke lesions, posed unique challenges. DWI channels, absent in qMRI simulations, were unseen during qATLAS/qSynth training. Nevertheless, qSynth significantly outperformed all models, including Synth, which

Table 3: Median results on the PLORAS dataset (N=263). Best score shown in bold, with second-best underlined and third-best in italics Student’s  $t$  distribution 95% confidence intervals given in brackets.

Modality	Model	Dice	HD95
T2w	Baseline	0.000 (0.000-0.004)	71.0 (66.3-75.8)
	qATLAS	0.035 (0.000-0.071)	<b>63.1 (56.7-69.4)</b>
	Synth	<i>0.117 (0.061-0.174)</i>	68.0 (62.4-73.7)
	Synth (+ real)	0.070 (0.014-0.125)	73.4 (68.0-78.8)
	qSynth	<u>0.177 (0.123-0.232)</u>	<i>65.2 (59.8-70.6)</i>
	qSynth (+ real)	<b>0.181 (0.127-0.234)</b>	63.8 (58.5-69.2)
FLAIR	Baseline	0.000 (0.000-0.001)	<b>66.5 (60.1-72.9)</b>
	qATLAS	0.000 (0.000-0.021)	70.2 (61.4-78.9)
	Synth	<i>0.170 (0.136-0.204)</i>	<u>76.5 (73.2-79.7)</u>
	Synth (+ real)	0.129 (0.095-0.164)	77.6 (74.3-80.8)
	qSynth	<b>0.239 (0.207-0.271)</b>	81.2 (77.9-84.6)
	qSynth (+ real)	<u>0.211 (0.181-0.241)</u>	79.1 (76.0-82.3)

could have trained on DWI-like data. qSynth achieved the highest Dice scores for T2w and FLAIR modalities, while both Synth and qSynth showed strong ensemble performance. For T1w, qATLAS and Synth achieved the best results. The dataset’s skull-stripped images likely conferred an advantage to Synth/qSynth models compared to other methods.

## 5 Conclusion

In this work, we introduced two novel qMRI-based synthetic data generation methods, qATLAS and qSynth, designed to advance domain-agnostic stroke lesion segmentation. Our results demonstrate that these approaches address distinct challenges in out-of-distribution data generalisation. The qATLAS model, which generates synthetic data from MPRAGE-derived qMRI maps, excels in T1-weighted data but struggles with other modalities. This limitation highlights the dependency on MPRAGE-derived maps, which may not capture the broader physiological diversity inherent in other sequences.

Conversely, the qSynth method, leveraging intensity priors from real qMRI data, consistently outperforms prior synthetic approaches in domain-agnostic settings. Its ability to incorporate physical realism into synthetic data generation proves critical for enhancing model generalisation across diverse imaging domains, demonstrating the value of physics-constrained augmentation in segmentation tasks.

Looking ahead, combining qSynth with domain adaptation techniques could establish a robust foundation model adaptable across modalities. Incorporating multiple simulated sequences using strategies like weakly supervised learning [21] may further broaden applicability, particularly for pathologies commonly imaged with specific modality combinations. Additionally, advances in deep generative modelling could refine the qMRI generator, while translating multi-modal data into qMRI maps could improve the representation of physiological variability.

Table 4: Median results on the ISLES2015 dataset (N=28). Best score shown in bold, with second-best underlined and third-best in italics Student’s  $t$  distribution 95% confidence intervals given in brackets.

Modality	Model	Dice	HD95
T1w	Baseline	0.000 (0.000-0.064)	69.8 (30.0-109.7)
	qATLAS	0.252 (0.142-0.363)	<b>51.5 (40.0-63.0)</b>
	Synth	<b>0.304 (0.213-0.396)</b>	58.6 (48.5-68.6)
	Synth (+ real)	<i>0.110 (0.012-0.208)</i>	52.5 (29.9-75.0)
	qSynth	0.002 (0.000-0.078)	56.3 (19.6-93.1)
	qSynth (+ real)	0.013 (0.000-0.087)	<i>56.3 (17.8-94.8)</i>
T2w	Baseline	0.000 (0.000-0.002)	63.1 (57.8-68.4)
	qATLAS	0.082 (0.000-0.170)	<b>59.4 (43.3-75.4)</b>
	Synth	0.074 (0.000-0.184)	72.3 (65.7-78.9)
	Synth (+ real)	<i>0.111 (0.007-0.216)</i>	75.0 (68.4-81.7)
	qSynth	0.222 (0.114-0.329)	<i>66.1 (58.3-73.8)</i>
	qSynth (+ real)	<b>0.225 (0.117-0.333)</b>	67.7 (59.8-75.6)
FLAIR	Baseline	0.000 (0.000-0.000)	71.8 (38.5-105.2)
	qATLAS	0.004 (0.000-0.052)	65.8 (51.2-80.5)
	Synth	0.372 (0.255-0.489)	56.1 (49.5-62.7)
	Synth (+ real)	0.212 (0.085-0.340)	<b>56.1 (38.7-73.4)</b>
	qSynth	<b>0.392 (0.281-0.504)</b>	<i>64.5 (55.0-73.9)</i>
	qSynth (+ real)	<i>0.332 (0.226-0.439)</i>	66.0 (57.5-74.5)
DWI	Baseline	0.000 (0.000-0.000)	83.7 (57.3-110.2)
	qATLAS	0.001 (0.000-0.027)	<i>75.9 (71.2-80.6)</i>
	Synth	<i>0.082 (0.000-0.168)</i>	83.7 (76.3-91.0)
	Synth (+ real)	0.056 (0.000-0.144)	84.9 (77.2-92.6)
	qSynth	<b>0.243 (0.155-0.331)</b>	75.7 (67.9-83.5)
	qSynth (+ real)	0.162 (0.076-0.249)	<b>74.4 (67.1-81.7)</b>
Ensemble	Baseline	0.000 (0.000-0.000)	256.0 (0.0-256.0)
	qATLAS	0.048 (0.000-0.123)	60.2 (25.9-94.4)
	Synth	0.272 (0.157-0.388)	<i>60.1 (49.7-70.5)</i>
	Synth (+ real)	<b>0.423 (0.302-0.545)</b>	<b>47.3 (24.2-70.4)</b>
	qSynth	<i>0.335 (0.222-0.448)</i>	67.5 (59.7-75.3)
	qSynth (+ real)	0.404 (0.284-0.524)	56.3 (48.1-64.5)

To strengthen domain generalisation, treating forward simulations as unique domains could ensure consistent performance transitions from simulated to real data. While this study focused on stroke lesions, these methods have potential applications in other pathologies, such as glioblastoma, where preserving fine-grained contrasts between tumour subregions is critical. Further, providing modality-specific context—whether at a coarse level (e.g., T2w vs. T1w) or fine-grained (e.g., echo times, relaxation rates)—as input conditioning for segmentation networks may allow customisation for specific acquisition protocols.

An important extension is to explore whether the benefits of qMRI-based synthesis extend to other domains where synthetic data has been impactful, such as healthy brain parcellation [3], and super-resolution [15].

Overall, this study highlights the potential of physics-constrained qMRI augmentation for domain-agnostic segmentation. By ensuring synthetic images adhere to MRI physics, these methods enhance robustness and generalisability, paving the way for future innovations in medical imaging research and practice.

## 6 Acknowledgement

LC is supported by the EPSRC-funded UCL Centre for Doctoral Training in Intelligent, Integrated Imaging in Healthcare (i4health) (EP/S021930/1), and the Wellcome Trust (203147/Z/16/Z and 205103/Z/16/Z). This research was supported by NVIDIA and used NVIDIA RTX A6000 48GB.

## Bibliography

- [1] Baur, C., Wiestler, B., Albarqouni, S., et al.: Fusing unsupervised and supervised deep learning for white matter lesion segmentation. In: Cardoso, M.J., Feragen, A., Glocker, B., et al. (eds.) Proceedings of The 2nd International Conference on Medical Imaging with Deep Learning. Proceedings of Machine Learning Research, vol. 102, pp. 63–72. PMLR (08–10 Jul 2019), <https://proceedings.mlr.press/v102/baur19a.html>
- [2] Billot, B., Cerri, S., Leemput, K.V., et al.: Joint segmentation of multiple sclerosis lesions and brain anatomy in MRI scans of any contrast and resolution with CNNs. In: 2021 IEEE 18th International Symposium on Biomedical Imaging (ISBI). IEEE (Apr 2021). <https://doi.org/10.1109/isbi48211.2021.9434127>
- [3] Billot, B., Greve, D.N., Puonti, O., et al.: SynthSeg: Segmentation of brain MRI scans of any contrast and resolution without retraining. *Medical Image Analysis* **86**, 102789 (May 2023). <https://doi.org/10.1016/j.media.2023.102789>
- [4] Borges, P., Fernandez, V., Tudosiu, P.D., et al.: Unsupervised Heteromodal Physics-Informed Representation of MRI Data: Tackling Data Harmonisation, Imputation and Domain Shift, p. 53–63. Springer Nature Switzerland (2023). [https://doi.org/10.1007/978-3-031-44689-4\\_6](https://doi.org/10.1007/978-3-031-44689-4_6), [http://dx.doi.org/10.1007/978-3-031-44689-4\\_6](http://dx.doi.org/10.1007/978-3-031-44689-4_6)
- [5] Borges, P., Shaw, R., Varsavsky, T., et al.: Acquisition-invariant brain mri segmentation with informative uncertainties (2021)
- [6] Brudfors, M., Balbastre, Y., Flandin, G., et al.: Flexible Bayesian Modelling for Nonlinear Image Registration, p. 253–263. Springer International Publishing (2020). [https://doi.org/10.1007/978-3-030-59716-0\\_25](https://doi.org/10.1007/978-3-030-59716-0_25)
- [7] Cardoso, M.J., Li, W., Brown, R., et al.: Monai: An open-source framework for deep learning in healthcare (2022)
- [8] Chalcraft, L., Pappas, I., Price, C.J., Ashburner, J.: Synthetic data for robust stroke segmentation (2024), <https://arxiv.org/abs/2404.01946>
- [9] Chen, S., Ma, K., Zheng, Y.: Med3d: Transfer learning for 3d medical image analysis (2019)
- [10] Dorent, R., Kujawa, A., Ivory, M., et al.: Crossmoda 2021 challenge: Benchmark of cross-modality domain adaptation techniques for vestibular schwannoma and cochlea segmentation. *Medical Image Analysis* **83**, 102628 (Jan 2023). <https://doi.org/10.1016/j.media.2022.102628>, <http://dx.doi.org/10.1016/j.media.2022.102628>
- [11] Gibson, M., Newman-Norlund, R., Bonilha, L., Fridriksson, J., Hickok, G., Hillis, A.E., den Ouden, D.B., Rorden, C.: The Aphasia Recovery Cohort, an open-source chronic stroke repository. *Scientific Data* **11**(1), 1–8 (2024). <https://doi.org/10.1038/s41597-024-03819-7>, <http://dx.doi.org/10.1038/s41597-024-03819-7>

- [12] Gudbjartsson, H., Patz, S.: The rician distribution of noisy mri data. *Magnetic Resonance in Medicine* **34**(6), 910–914 (Dec 1995). <https://doi.org/10.1002/mrm.1910340618>, <http://dx.doi.org/10.1002/mrm.1910340618>
- [13] He, K., Zhang, X., Ren, S., Sun, J.: Delving deep into rectifiers: Surpassing human-level performance on ImageNet classification (2015)
- [14] Hendrycks, D., Gimpel, K.: Gaussian error linear units (gelus) (2023)
- [15] Iglesias, J.E., Billot, B., Balbastre, Y., Magdamo, C., Arnold, S.E., Das, S., Edlow, B.L., Alexander, D.C., Golland, P., Fischl, B.: Synthsr: A public ai tool to turn heterogeneous clinical brain scans into high-resolution t1-weighted images for 3d morphometry. *Science Advances* **9**(5) (Feb 2023). <https://doi.org/10.1126/sciadv.add3607>, <http://dx.doi.org/10.1126/sciadv.add3607>
- [16] Isensee, F., Jaeger, P.F., Kohl, S.A.A., et al.: nnU-Net: a self-configuring method for deep learning-based biomedical image segmentation. *Nature Methods* **18**(2), 203–211 (Dec 2020). <https://doi.org/10.1038/s41592-020-01008-z>
- [17] Johnson, L., Newman-Norlund, R., Teghipco, A., et al.: Progressive lesion necrosis is related to increasing aphasia severity in chronic stroke. *NeuroImage: Clinical* **41** (1 2024). <https://doi.org/10.1016/j.nicl.2024.103566>
- [18] Liew, S.L., Lo, B.P., Donnelly, M.R., et al.: A large, curated, open-source stroke neuroimaging dataset to improve lesion segmentation algorithms. *Scientific Data* **9**(1) (Jun 2022). <https://doi.org/10.1038/s41597-022-01401-7>
- [19] Loshchilov, I., Hutter, F.: Decoupled weight decay regularization (2019)
- [20] Maier, O., Menze, B.H., von der Gabelntz, J., et al.: ISLES 2015 - a public evaluation benchmark for ischemic stroke lesion segmentation from multispectral MRI. *Medical Image Analysis* **35**, 250–269 (Jan 2017). <https://doi.org/10.1016/j.media.2016.07.009>
- [21] Patel, G., Dolz, J.: Weakly supervised segmentation with cross-modality equivariant constraints (2022)
- [22] de la Rosa, E., Reyes, M., Liew, S.L., Hutton, A., Wiest, R., Kaesmacher, J., Hanning, U., Hakim, A., Zubal, R., Valenzuela, W., Robben, D., Sima, D.M., Anania, V., Brys, A., Meakin, J.A., Mickan, A., Broocks, G., Heitkamp, C., Gao, S., Liang, K., Zhang, Z., Siddiquee, M.M.R., Myronenko, A., Ashtari, P., Huffel, S.V., su Jeong, H., ho Yoon, C., Kim, C., Huo, J., Ourselin, S., Sparks, R., Clèrigues, A., Oliver, A., Lladó, X., Chalcraft, L., Pappas, I., Bertels, J., Heylen, E., Moreau, J., Hatami, N., Frindel, C., Qayyum, A., Mazher, M., Puig, D., Lin, S.C., Juan, C.J., Hu, T., Boone, L., Goubran, M., Liu, Y.J., Wegener, S., Kofler, F., Ezhov, I., Shit, S., Petzsche, M.R.H., Menze, B., Kirschke, J.S., Wiestler, B.: A robust ensemble algorithm for ischemic stroke lesion segmentation: Generalizability and clinical utility beyond the isles challenge (2024), <https://arxiv.org/abs/2403.19425>
- [23] Tabelow, K., Balteau, E., Ashburner, J., et al.: hmri – a toolbox for quantitative mri in neuroscience and clinical research. *NeuroImage* **194**, 191–210

- (Jul 2019). <https://doi.org/10.1016/j.neuroimage.2019.01.029>, <http://dx.doi.org/10.1016/j.neuroimage.2019.01.029>
- [24] Ulyanov, D., Vedaldi, A., Lempitsky, V.: Instance normalization: The missing ingredient for fast stylization (2017)
- [25] Varadarajan, D., Bouman, K.L., van der Kouwe, A., et al.: Unsupervised learning of mri tissue properties using mri physics models (2021)
- [26] Wang, D., Shelhamer, E., Liu, S., et al.: Tent: Fully test-time adaptation by entropy minimization (2021)
- [27] Wang, G., Li, W., Ourselin, S., Vercauteren, T.: Automatic Brain Tumor Segmentation Using Convolutional Neural Networks with Test-Time Augmentation, p. 61–72. Springer International Publishing (2019). [https://doi.org/10.1007/978-3-030-11726-9\\_6](https://doi.org/10.1007/978-3-030-11726-9_6), [http://dx.doi.org/10.1007/978-3-030-11726-9\\_6](http://dx.doi.org/10.1007/978-3-030-11726-9_6)
- [28] Zhang, R., Isola, P., Efros, A.A., et al.: The unreasonable effectiveness of deep features as a perceptual metric (2018)